Author(s): Obrezkov, Leonid; Bozorgmehri, Babak; Finni, Taija; Matikainen, Marko K.

Title: Approximation of pre-twisted Achilles sub-tendons with continuum-based beam elements
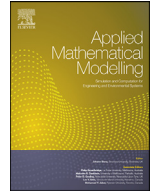
Please cite the original version:

Obrezkov, L., Bozorgmehri, B., Finni, T., & Matikainen, M. K. (2022). Approximation of pre-twisted Achilles sub-tendons with continuum-based beam elements. Applied Mathematical Modelling, 112, 669-689. https://doi.org/10.1016/j.apm.2022.08.014

Approximation of pre-twisted Achilles sub-tendons with continuum-based beam elements

Leonid Obrezkov [a,*], Babak Bozorgmehri [a,b,c], Taija Finni [d], Marko K. Matikainen [a]

[a] Mechanical Engineering, LUT University, Yliopistonkatu 34, Lappeenranta 53850, Finland
[b] Department of Mechanical Engineering, KU Leuven, Heverlee 3001, Belgium
[c] DMMS, Flanders Make @ KU Leuven, Belgium
[d] Faculty of Sport and Health Sciences, University of Jyväskylä, Jyväskylä, Finland

ARTICLE INFO

ABSTRACT

Achilles sub-tendons are materially and geometrically challenging structures that can nearly undergo around 15% elongation from their pre-twisted initial states during physical activities. Sub-tendons' cross-sectional shapes are subject-specific, varying from simple to complicated. Therefore, the Achilles sub-tendons are often described by three-dimensional elements that lead to a remarkable number of degrees of freedom. On the other hand, the continuum-based beam elements in the framework of the absolute nodal coordinate formulation have already been shown to be a reliable and efficient replacement for the three-dimensional continuum elements in some special problems. So far, that element type has been applied only to structures with a simple cross-section geometry. To computationally efficiently describe a pre-twisted Achilles sub-tendon with a complicated cross-section shape, this study will develop a continuum-based beam element based on the absolute nodal coordinate formulation with an arbitrary cross-section description. To demonstrate the applicability of the developed beam element to the Achilles sub-tendons, 16 numerical examples are considered. During these numerical tests, the implemented cross-section descriptions agreed well with the reference solutions and led to faster convergence rates in comparison with the solutions provided by commercial finite element codes. Furthermore, it is demonstrated that in the cases of very complicated cross-sectional forms, the commercial software ANSYS provides inflated values for the elongation deformation in comparison with ABAQUS (about 6.2%) and ANCF (about 9.4%). Additionally, the numerical results reveal a possibility to model the whole sub-tendons via coarse discretization with high accuracy under uniaxial loading. This demonstrates the huge potential for use in biomechanics and also in multibody applications, where the arbitrary cross-section of beam-like structures needs to be taken into account.

© 2022 The Author(s). Published by Elsevier Inc.
This is an open access article under the CC BY license
(http://creativecommons.org/licenses/by/4.0/)

1. Introduction

The Achilles tendon is one of the most important tendons of the human body. As the largest and strongest tendon, it has enormous energy-storing abilities and plays a key role during movements such as running or jumping. It is also character-

---

ized by its high tensile strength, non-linear deformations, up to 15% from its initial state [1], and viscoelastic properties [2]. Its analysis in the framework of computational modelling has been under investigation over the past decade, and its achievements have received wide attention in the literature [3]. However, the analysis itself is challenging because the exact form, functions and inner structure of the Achilles are very complex: a pre-twisted anisotropic structure consisting of several sub-tendons, sliding one around another, where each of them has a sophisticated geometrical shape with differential motor control from the muscles [4–6]. Additional factors affecting the mechanical behaviour may include age, gender and genetics contributions [7]. Thus, it is not surprising that most of the studies simplify the Achilles tendon models by considering only some features attributed to the tendon. For example, authors may consider it as an isotropic solid [3,8,9], treat it as a single non-divided structure [10,11], or ignore its pre-twisted configuration [12]. However, each of these approaches has a significant effect on the final results. The work of Handsfield et al. [4], the authors conclude that the twist between 15 and 45 degrees optimizes rupture load and stress distributions. Kinugasa et al. [10] have demonstrated the importance of the fiber orientation for the Achilles tendon. Hansen et al. [7] have shown the tendon cross-section geometry is an important determinant of injury risk even if the internal division of the tendon is omitted. On the other hand, the inclusion of all the features simultaneously leads to a computationally demanding model. A possible solution without resorting to physical or geometrical simplifications is the utilization of more efficient and robust approaches.

Multibody system dynamics offers various computer-based approaches for generating and solving equations of motion of complex mechanical systems. About two decades ago, the absolute nodal coordinate formulation (ANCF) was introduced to describe large deformations within beam-, plate- or shell-type structures in multibody applications [13,14]. Since then, the ANCF has actively been developed and utilized by the multibody community for various large deformation problems [15–18]. The ANCF is a nonlinear finite element approach in which beam and plate/shell element cross-sections can be deformable. The key idea behind ANCF-based elements is that having element nodal coordinates at hand, including the position vector derivatives, i.e., slope vectors, the kinematics of flexible spatial bodies can be described using polynomial based spatial shape functions [19]. Generally speaking, the use of components of the deformation gradient as degrees of freedom (DOFs) can be seen as a trademark of the ANCF. As a result, in specific situations, ANCF-based elements demonstrate computational efficiency in comparison with conventional three-dimensional finite continuum elements for the modelling of the beam- and plate/shell-like structures [17,20,21].

During the past decades, several ANCF elements have been proposed based on the various types of displacement interpolations and descriptions of internal energy [20,22,23]. So far, ANCF-based beam and plate/shell elements can be categorized mainly into three groups with respect to the number of slopes (first-order) vectors and higher-order slope vector derivatives: low-order, fully-parameterized, and higher-order elements. In the low-order elements (see examples in Nachbagauer et al. [16], Kerkkänen et al. [24], Garcìa-Vallejo et al. [25]), the displacement interpolation is accomplished in a manner where all slope vectors are not taken into account in the kinematics description. In the fully-parameterized elements (see example studies [26–28]), all first-order slope vectors are utilized. On the downside, the usage of all slope vectors leads to a higher computational cost in comparison to the low-order elements [20]. Additionally, the above-mentioned ANCF-based beam elements can either be defined with respect to the material laws based on general continuum mechanics, i.e., using full three-dimensional elasticity, or alternatively, with respect to structural mechanics-based approaches. For higher-order ANCF elements [29–31], higher than first-order derivatives are used in displacement interpolation to describe the cross-section deformation more precisely [32]. On the downside, in the case of the higher-order ANCF elements, internal energy needs to be derived based on general continuum mechanics.

Despite great efforts that have been devoted to introducing a variety of ANCF elements and demonstrating their usability in solving various problems, their applications have solely been limited to beams with simple geometries, such as cylindrical or parallelepiped structures [15,17,20,33,34]. In [35,36], a subdomain integration method was introduced to capture the local surface geometry. The drawback of this numerical area integration method is that in the case of complex shapes, the body has to be divided into a significant number of subdomains, and each requires different integration methods.

The aim of the study is to provide a general description for beam-like structures with an arbitrary cross-section in the framework of the ANCF, and subsequently, describe the Achilles sub-tendons. For this reason, we study the usability of the method based on a numerical integration scheme via Greens integral formula [37,38] for a three-node quadratic continuum-based ANCF beam element [16]. The advantage of this method is the implementation of the Gaussian integration scheme for the whole domain with piece-wise regular boundaries. That reduces the approximation error, which appears due to the splitting of the domain into the subdomains, and requires fewer degrees of freedom, increasing computational efficiency.

2. The kinematics of an ANCF beam element

In this section, the kinematics of a three-node quadratic ANCF beam element (denoted by ANCF 3333c) proposed by Nachbagauer et al. [16] is briefly reviewed. These four numbers in the element name *abcd* have the following meaning: *a* is the dimension of the element, *b* denotes the number of nodes, *c* is the number of vectors used in the approximations, and *d* is the polynomial basis used to approximate all three dimensions [20]. The position vector field at the current configuration is defined as $\mathbf{r} = \mathbf{r}(x, y, z)$, with the position vector in the initial configuration being $\bar{\mathbf{r}}$; see Fig. 1. The connection between the position and displacement field vectors can be written as:
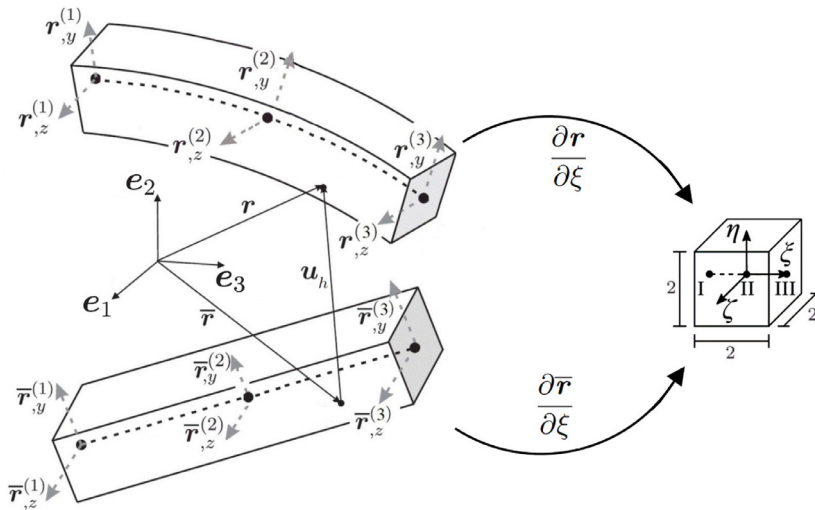
$$\mathbf{r} = \bar{\mathbf{r}} + \mathbf{u}_h, \tag{1}$$

Fig. 1. ANCF 3333c beam element with the position vector r of an arbitrary particle p in the current and reference configurations, respectively [16,17].

where vector $\boldsymbol{u}_h$ describes a displacement field. Thus, the position and displacement fields of isoparametric finite elements can be interpolated in the form:

$$\boldsymbol{r}(x, y, z) = \mathbf{N}_m(x, y, z)\boldsymbol{q}, \tag{2}$$

$$\boldsymbol{u}_h(x, y, z) = \mathbf{N}_m(x, y, z)\boldsymbol{u}, \tag{3}$$

where $\mathbf{N}_m$ is a shape function matrix, $\boldsymbol{u}$ is a vector of nodal displacements, and $\boldsymbol{q}$ is a vector of nodal position coordinates that in the case of the element 3333c for the ith node read as follows:

$$\boldsymbol{q}_i = \left[\boldsymbol{r}^{i^T} \boldsymbol{r}_{,y}^{i^T} \boldsymbol{r}_{,z}^{i^T}\right]^T. \tag{4}$$

Hence, shorthand symbols are used as follows:

$$\boldsymbol{r}_{,\alpha}^i = \frac{\partial \boldsymbol{r}^i}{\partial \alpha}, \alpha = \{y, z\}. \tag{5}$$

A local bi-normalized coordinate system $\boldsymbol{\xi} = \{\xi, \eta, \zeta\}$ is formed as illustrated in Fig. 1, with the range for the local coordinates $[-1, 1]$. The position and nodal displacement vectors can, respectively, be expressed in terms of the bi-normalized coordinates as follows:

$$\begin{aligned}\boldsymbol{r}(\xi, \eta, \zeta) &= \mathbf{N}_m(\xi, \eta, \zeta)\boldsymbol{q}, \\ \boldsymbol{u}_h(\xi, \eta, \zeta) &= \mathbf{N}_m(\xi, \eta, \zeta)\boldsymbol{u},\end{aligned} \tag{6}$$

where the non-dimensional quantities are defined as follows:

$$\xi = \frac{x}{\ell_x}, \quad \eta = \frac{y}{\ell_y}, \quad \zeta = \frac{z}{\ell_z}, \tag{7}$$

where l_x, l_y and l_z are the physical dimensions of the element. The shape function matrix in the case of the ANCF 3333c takes the following form:

$$\mathbf{N}_m(\xi, \eta, \zeta) = [N_1 \mathbf{I} N_2 \mathbf{I} N_3 \mathbf{I} \ldots N_9 \mathbf{I}], \tag{8}$$

where $\mathbf{I}$ is an 3×3 identity matrix, and shape functions can be written as

$$N_1 = \frac{1}{2}\xi(\xi - 1) \quad N_2 = \frac{1}{4}l_y\xi\eta(\xi - 1) \quad N_3 = \frac{1}{4}l_z\xi\zeta(\xi - 1)$$

$$N_4 = 1 - \xi^2 \qquad N_5 = \frac{1}{2}l_y\eta(1 - \xi^2) \qquad N_6 = \frac{1}{2}l_z\zeta(1 - \xi^2)$$

$$N_7 = \frac{1}{2}\xi(\xi + 1) \quad N_8 = \frac{1}{4}l_y\xi\eta(\xi + 1) \quad N_9 = \frac{1}{4}l_z\xi\zeta(\xi + 1).$$

From (6), the deformation gradient $\mathbf{F}$ can be written as:

$$\mathbf{F} = \frac{\partial \boldsymbol{r}}{\partial \overline{\boldsymbol{r}}} = \frac{\partial \boldsymbol{r}}{\partial \boldsymbol{\xi}}\left(\frac{\partial \overline{\boldsymbol{r}}}{\partial \boldsymbol{\xi}}\right)^{-1} = \mathbf{I} + \frac{\partial \boldsymbol{u}_h}{\partial \boldsymbol{\xi}}\left(\frac{\partial \overline{\boldsymbol{r}}}{\partial \boldsymbol{\xi}}\right)^{-1}. \tag{9}$$

The determinant of $\mathbf{F}$ defines the volume ratio of the element, and in this regard, considering continuity, it can be said that

$$J = \det \mathbf{F} > 0. \tag{10}$$

3. Equilibrium equation

In this section, we derive the weak equilibrium equation as follows:

$$\boldsymbol{F}_{ext}\delta\boldsymbol{q} + \boldsymbol{F}_{int}\delta\boldsymbol{q} = 0, \tag{11}$$

where the vectors $\boldsymbol{F}_{ext}$ and $\boldsymbol{F}_{int}$ are the vectors of external and internal forces, respectively, and $\delta\boldsymbol{q}$ is a variation of nodal position coordinates. The latter one can be rewritten as

$$\boldsymbol{F}_{int} = \mathbf{S} : \frac{\partial \mathbf{E}}{\partial \boldsymbol{q}}, \tag{12}$$

where $\mathbf{S}$ is the second Piola–Kirchhoff stress, and $\mathbf{E}$ is the Green–Lagrange strain given as

$$\mathbf{E} = \frac{1}{2}\left(\mathbf{F}^T \cdot \mathbf{F} - \mathbf{I}\right). \tag{13}$$

In this work, we deal with the description of biomaterials, which are often considered as incompressible hyperelastic solids [39]. This assumption is reasonable, as the biological tissues contain a significant amount of water [40] To obtain the form of the second Piola–Kirchhoff stress $\mathbf{S}$ for such solids, the Helmholtz free energy function Ψ is usually used. Then, following the common approach presented in Handsfield et al. [3], 4], Obrezkov et al. [17], Holzapfel and Gasser [41], Holzapfel and Ogden [42], the multiplicative decomposition of the deformation into dilational (volumetric) and distortion (isochoric) parts is considered:

$$\mathbf{F} = J^{\frac{1}{3}}\overline{\mathbf{F}}, \tag{14}$$

where $\overline{\mathbf{F}}$ represents the deviatoric part with $\det \overline{\mathbf{F}} = 1$. Therefore, the right and left Cauchy–Green deformation tensors are

$$\overline{\mathbf{C}} = \overline{\mathbf{F}}^T \cdot \overline{\mathbf{F}}, \overline{\mathbf{B}} = \overline{\mathbf{F}} \cdot \overline{\mathbf{F}}^T. \tag{15}$$

In the isotropic case, all deformations can be defined as a function of the right Cauchy–Green tensor. However, biomaterials often demonstrate anisotropic behaviour. To describe anisotropy, the preferable deformation direction in the current configuration can be defined via a vector field $\boldsymbol{a}$ at each point. In the initial configuration, this vector is unit one and defined as $\boldsymbol{a}_0$, and the connection between them described as $\boldsymbol{a} = \overline{\mathbf{F}} \cdot \boldsymbol{a}_0$. The square of the preferable direction vector extension is defined as follows:

$$\lambda_{\boldsymbol{a}_0}^2 = \overline{\mathbf{C}} : \mathbf{A}_0, \tag{16}$$

where $\mathbf{A}_0$ is a structural tensor of order two and takes the form $\mathbf{A}_0 = \boldsymbol{a}_0 \otimes \boldsymbol{a}_0$. Thus, the strain energy density for elastic materials reinforced by one family of fibers (preferred deformation direction) can be expressed as $\Psi = \Psi(\overline{\mathbf{C}}, \mathbf{A}_0, J)$. If necessary, the concept can be easily extended to several families of fibers. The additive split (14) leads to the following expression [43]:

$$\Psi = \overline{\Psi}(\overline{\mathbf{C}}, \mathbf{A}_0) + \Psi_{vol}(J), \tag{17}$$

where $\Psi_{vol}(J)$ is the volumetric part and $\overline{\Psi}(\overline{\mathbf{C}}, \mathbf{A}_0)$ is the isochoric part. In this work, the former is represented by a quadratic function:

$$\Psi_{vol} = \frac{d}{2}(J - 1)^2. \tag{18}$$

The experimental results [44] have demonstrated its possibility to adequately describe the volume change for slightly compressible solids in simple tensions. In (18), d is the penalty coefficient, which need to be large enough for imposing the incompressibility constraint. Further, the deviatoric part can be expressed via the invariants of the Cauchy–Green and structural tensors [41,42]:

$$\overline{\Psi} = \overline{\Psi}(\overline{I}_1, \overline{I}_2, \overline{I}_4, \overline{I}_5), \tag{19}$$

where

$$\begin{aligned}\overline{I}_1 = \mathrm{tr}\overline{\mathbf{C}}, \overline{I}_2 &= \tfrac{1}{2}\left(\mathrm{tr}\,\overline{\mathbf{C}}^2 + \mathrm{tr}^2\overline{\mathbf{C}}\right), \\ \overline{I}_4 &= \overline{\mathbf{C}} : \mathbf{A}_0, \overline{I}_5 = \overline{\mathbf{C}}^2 : \mathbf{A}_0.\end{aligned} \tag{20}$$

The total strain energy density Ψ for anisotropic materials can be written as

$$\Psi = \overline{\Psi}(\overline{I}_1, \overline{I}_2, \overline{I}_4, \overline{I}_5) + \Psi_{vol}(J). \tag{21}$$

Usually, for mathematical simplicity, $\overline{I_5}$ is mostly neglected. References [45–47] showed its importance for shear deformations, but for axial loading cases it can be omitted. It should also be remembered that $\overline{I_3} = \det\overline{\mathbf{C}} = 1$ does not have an effect on the function Ψ. The total second Piola–Kirchhoff stress is

$$\mathbf{S} = 2\frac{\partial\Psi}{\partial\mathbf{C}} = 2\frac{\partial\Psi}{\partial\overline{\mathbf{C}}} : \frac{\partial\overline{\mathbf{C}}}{\partial\mathbf{C}}. \tag{22}$$

Using the form of the strain energy density described in (21), (22) can be rewritten [17]:

$$\mathbf{S} = 2\frac{\partial\overline{\Psi}}{\partial\overline{\mathbf{C}}}\frac{\partial\overline{\mathbf{C}}}{\partial\mathbf{C}} + 2\frac{\partial\Psi_{vol}}{\partial J}\frac{\partial J}{\partial\mathbf{C}} = 2\left(\sum_k \frac{\partial\overline{\Psi}}{\partial\overline{I}_k}\frac{\partial\overline{I}_k}{\partial\overline{\mathbf{C}}}\right)\frac{\partial\overline{\mathbf{C}}}{\partial\mathbf{C}} + \frac{\partial\Psi_{vol}}{\partial J}J\mathbf{C}^{-1}. \tag{23}$$

Then, with (23), the expression for the total second Piola–Kirchhoff (12) can reach its final form

$$\mathbf{S} = \overline{\mathbf{S}} + \mathbf{S}_{vol}, \tag{24}$$

where the volumetric part from (18) is

$$\mathbf{S}_{vol} = d(J-1)J\mathbf{C}^{-1}, \tag{25}$$

where the form of $\overline{\mathbf{S}}$ depends on the material model.

4. Material models under consideration

This section presents the Neo–Hookean and GOH [48] material models, alongside the expressions for the deviatoric parts of the strain energy densities and the corresponding second Piola–Kirchhoff stress tensors. For hyperelasticity modelling of biological tissues, there are various material models [39]. The chosen models are the most used (see [3,4,7,12,41–43,48–50] etc.) because of their simplicity and the minimal required number of material parameters for their characterization. They are also implemented in various software programs, which allows independently verifying research. The presented choice helps to consider the material description from two points of view, such as isotropic and anisotropic solids. Material laws usually describe anisotropy with exponential functions, as in the so-called GOH model [39]. The first model is the Neo–Hookean one. The deviatoric part is

$$\overline{\Psi} = \frac{1}{2}c_{10}\left(\overline{I_1} - 3\right). \tag{26}$$

The corresponding deviatoric part of the second Piola–Kirchhoff stress has the form

$$\overline{\mathbf{S}} = 2c_{10}J^{-\frac{2}{3}}\left[\mathbf{I} - \frac{1}{3}\overline{I_1}\overline{\mathbf{C}}^{-1}\right]. \tag{27}$$

The next material model under consideration is the anisotropic GOH model [48]:

$$\overline{\Psi} = c_{10}\left(\overline{I_1} - 3\right) + \frac{c_1}{2c_2}\left(e^{c_2(\overline{I_4}-1)} - 1\right), \tag{28}$$

and the corresponding deviatoric part of the second Piola–Kirchhoff stress tensor is

$$\begin{aligned}\overline{\mathbf{S}} &= 2J^{-\frac{2}{3}}\left[c_{10}\mathbf{I} + \frac{c_1}{2}e^{c_2(\overline{I_4}-1)}\mathbf{A}_0\right] \\ &\quad -\frac{2}{3}J^{-\frac{2}{3}}\left[c_{10}\overline{I_1} + \frac{c_1}{2}e^{c_2(\overline{I_4}-1)}\overline{I_4}\right]\overline{\mathbf{C}}^{-1}. \end{aligned} \tag{29}$$

Despite the significant number of papers considering the analysis of tendons, material parameters may differ due to a lack of consensus [50,51]. Moreover, the aim of this paper is to present a tool for tendon description. Thus, the authors will use the parameter values provided in the papers that describe related models [12,50].

5. Gauss–Green cubature

Usually, the standard Gaussian quadrature integration scheme is used for calculations performed with ANCF elements [52]. The formula for the integration of any function $f(x, y)$ can be applied only to the rectangular Ω and, according to this scheme, has the following form:

$$\int_\Omega f(x, y)d\Omega = \sum_{i=1}^{n}\sum_{j=1}^{n} f\left(x_i, y_j\right)\mathsf{w}_i\mathsf{w}_j, \tag{30}$$

where $2n - 1$ is the polynomial exactness degree of function f over one of the axis line, and w is the so-called weight of the point. In the case of other simple cross-section types (circular, etc.), the formula (30) might be updated according to Abramowitz et al. [53]. In this work, we aim to overcome the limitation of simple geometry applications via a combination ANCF approach with an advanced integration scheme. Here, the method originally proposed by Sommariva and Vianello
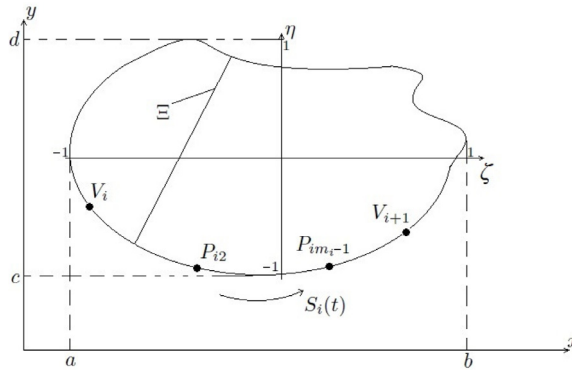
Fig. 2. An arbitrary domain in initial and local coordinate systems.

[38] is discussed for the arbitrary cross-section description. That allows to extend the application of a ANCF element to various fields where the arbitrary cross-section of beam-like structures needs to be taken into account. This method allows avoiding splitting the area into subdomains, as it does in standard FE approximations with three-dimensional elements, thus minimizing the number of elements and approximation errors.

Let us consider a closed domain Ω, which has a piece-wise border $\partial\Omega$ with points V_i on it:

$$V_i = (\alpha_i, \beta_i), i = 1, \ldots, \varphi,$$
$$\partial\Omega = [V_1, V_2] \cup [V_2, V_3] \cup \ldots \cup [V_\varphi, V_1]. \tag{31}$$

Moreover, the lines $[V_i, V_{i+1}]$ have several additional control points, such as $P_{i1} = V_i, P_{i2}, \ldots, P_{im_i} = V_{i+1}$, or in the bi-normalized coordinates as $P_{i1}^\xi = V_i^\xi, \ldots, P_{im_i}^\xi = V_{i+1}^\xi$. Subsequently, a parametrization is recalled; for example, the cumulative chordal formula [38]:

$$[\alpha_{ij}^\xi, \beta_{ij}^\xi] = \left[0, \sum_{j=1}^{m_i-1} \Delta t_{ij}\right], \mid \Delta t_{ij} \mid = \mid P_{ij+1}^\xi - P_{ij}^\xi \mid, j = 1, \ldots, m_i - 1.$$

Then, each line $[V_i^\xi, V_{i+1}^\xi]$ is tracked by a spline curve $S_i(t) = (S_{i1}(t), S_{i2}(t))$ degree of p_i, where $p_i \leq m_i - 1$, (Fig. 2).

Then the cubature formula with the $2n - 1$ polynomial exactness degree over the Ω domain has the form

$$I_{2n-1} = \sum_{\lambda \in \Lambda_{2n-1}} w_\lambda f(\eta_\lambda, \zeta_\lambda), \tag{32}$$

where

$$\Lambda_{2n-1} = \{\lambda = (i, j, k, h) : 1 \leqslant i \leqslant \varphi, 1 \leqslant j \leqslant m_i - 1,$$

$$1 \leqslant k \leqslant n_i, 1 \leqslant h \leqslant n\},$$

and w_λ, η_λ and ζ_λ are:

$$\eta_\lambda = \frac{S_{i1}(q_{ijk}) - \Xi}{2} \tau_h^n + \frac{S_{i1}(q_{ijk}) + \Xi}{2},$$

$$\zeta_\lambda = S_{i2}(q_{ijk}),$$

$$w_\lambda = \frac{\Delta t_{ij}}{4} \omega_k^{n_i} \omega_h^n (S_{i1}(q_{ijk}) - \Xi) \frac{dS_{i2}(t)}{dt} \mid_{t=q_{ijk}},$$

$$q_{ijk} = \frac{\Delta t_{ij}}{2} \tau_k^{n_i} + \frac{t_{ij+1} + t_{ij}}{2}, \Delta t_{ij} = t_{ij+1} - t_{ij},$$

$$n_i = \begin{cases} np_i + p_i/2, & p_i \text{ is even,} \\ np_i + (p_i + 1)/2, & p_i \text{ is odd.} \end{cases}$$

Thus, only $\tau_k^{n_i}$, $\omega_k^{n_i}$ and Ξ need to be defined. Ξ is an arbitrary straight line

$$\Omega \subseteq \mathbb{R}^2 = [a, b] \times [c, d], \Xi(\eta) \in [a, b], \eta \in [c, d].$$

Table 1
Border and control points of the square domain example in the initial and bi-normalized coordinate systems .

i	V_i	P_{i1}	V_i^ξ	P_{i1}^ξ
1	$(-0.05, -0.05)$	$(0, -0.05)$	$(-1, -1)$	$(0, -1)$
2	$(0.05, -0.05)$	$(0.05, 0)$	$(1, -1)$	$(1, 0)$
3	$(0.05, 0.05)$	$(0, 0.05)$	$(1, 1)$	$(0, 1)$
4	$(-0.05, 0.05)$	$(-0.05, 0)$	$(-1, 1)$	$(-1, 0)$

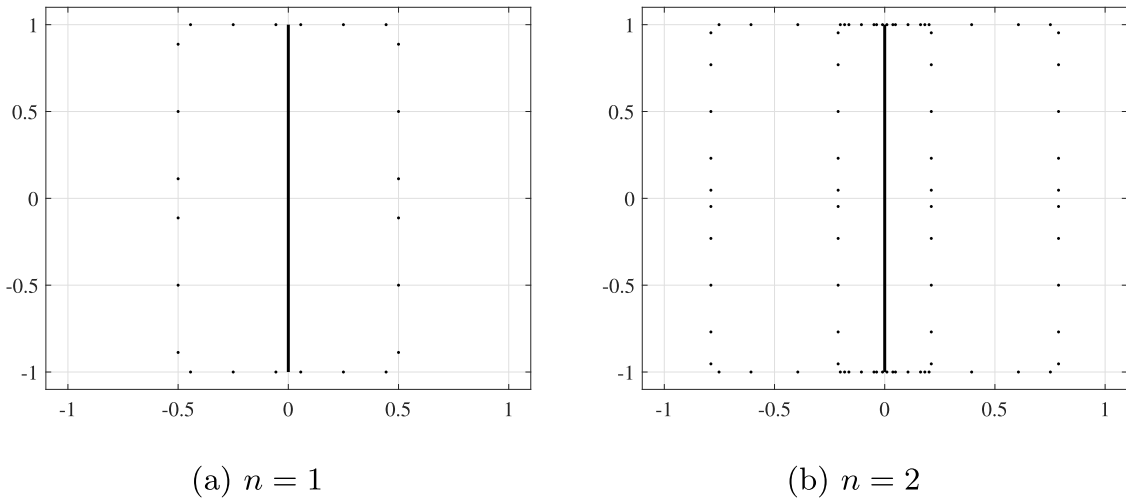(a) $n = 1$ (b) $n = 2$

Fig. 3. Examples of integration points from Tables 2 and 3 for the whole domain with different polynomial exactness degrees n given in the local coordinate system.

Table 2
The integration points for the side $i = 2$ of the square domain with polynomial exactness degree $2n - 1 = 1$; spline degree $p_2 = 2$.

ω_λ	η_λ	ζ_λ
0.2778	0.5	-0.1127
0.4444	0.5	-0.5
0.2778	0.5	-0.8873
0.2778	0.5	0.8873
0.4444	0.5	0.5
0.2778	0.5	0.1127

The choice of Ξ does not have any influence. However, it is necessary in obtaining the nodes and weights relative to it. $\tau_k^{n_i}$, $\omega_k^{n_i}$ are the nodes and weights, respectively, of the Gauss–Legendre quadrature formula of the exactness degree $2n_i - 1$ on $[-1, 1]$.

As an example, the method is applied to the square domain with a side length of 0.1 m. Each side of the square is described via three points; see Table 1. Therefore, we have $i = 4$ and $m_i = 3$.

Applying the algorithm to, for example, the second side, we have: $[\alpha_{2j}^\xi, \beta_{2j}^\xi] = [(0, 0), (0, 1), (0, 2)]$, $j = 1, 2, 3$, $p_2 \leq m_2 - 1 = 2$. Then, we apply a spline interpolation to the sequence of points $[\alpha_{2j}^\xi, \beta_{2j}^\xi]$ to obtain the curves $S_2(t) = (S_{21}(t), S_{22}(t))$. Assuming $n = 1$ (however, this number can be arbitrarily large), we obtain $n_2 = 3$. The next step is to determinate the Ξ line. After assuming $\Xi(\eta) = 0$, the following sequence of points is obtained:

The point coordinates and their weights for the sides 1, 3 and 4 can be obtained similarly, and the result can be seen in Fig. 3(a). Assuming $n = 2$, we can obtain $n_2 = 5$ and by repeating the whole procedure again, we get Table 3 and Fig. 3(b).

Thus, the substitution of the points' coordinates multiplied by their weights (e.g. Fig. 3(a)) into deformation characteristic functions described in Section 3, which are in their turn based on the kinematics presented in Section 2, enables obtaining the deformation of any arbitrary cross-section beam via a ANCF continuum-based beam element description.

Table 3
The integration points for the side $i = 2$ of the square domain from Table 1, with the polynomial exactness degree $2n - 1 = 3$ and spline degree $p_2 = 2$.

ω_λ	η_λ	ζ_λ	ω_λ	η_λ	ζ_λ
0.0592	0.7887	−0.0469	0.0592	0.2113	−0.0469
0.1197	0.7887	−0.2308	0.1197	0.2113	−0.2308
0.1422	0.7887	−0.5000	0.1422	0.2113	−0.5000
0.1197	0.7887	−0.7692	0.1197	0.2113	−0.7692
0.0592	0.7887	−0.9531	0.0592	0.2113	−0.9531
0.0592	0.7887	0.9531	0.0592	0.2113	0.9531
0.1197	0.7887	0.7692	0.1197	0.2113	0.7692
0.1422	0.7887	0.5000	0.1422	0.2113	0.5000
0.1197	0.7887	0.2308	0.1197	0.2113	0.2308
0.0592	0.7887	0.0469	0.0592	0.2113	0.0469

6. Analytical solutions for beams

This section derives analytical solutions for isotropic and anisotropic beams with rectangular and arbitrary cross-sections. It is assumed that, structures have no holes or other imperfections.

6.1. Analytical solutions for the rectangular beams

This section derives the analytical solution for a rectangular beam from the incompressible material model. The volume of the beam in the initial configuration denoted as V for rectangular bars can be expressed as

$$V = HWL, \tag{33}$$

where L is the length (in the longitudinal direction) of the beam-like structure, and H and W are the height and the width of the beam (in the transverse directions), respectively. After the application of the tensile load N, we assume that initial length L changes γ times; thus, in the deformable state the length is $l = \gamma L$. As we consider the beam as an incompressible solid, the volume does not change. Hereafter, we have $w = \frac{W}{\sqrt{\gamma}}$ and $h = \frac{H}{\sqrt{\gamma}}$, where h and w are the dimensions in the actual configuration. The Cauchy stress tensor for incompressible solids is [42]:

$$\sigma = -p\mathbf{I} + 2\mathbf{F}\left(\frac{\partial \Psi}{\partial \mathbf{C}}\right)\mathbf{F}^T, \tag{34}$$

where Ψ is the potential density function (17), and p is a function of hydrostatic stress, which is not determined. $\mathbf{C} = \mathbf{F}^T \cdot \mathbf{F}$ and $\mathbf{B} = \mathbf{F} \cdot \mathbf{F}^T$ are, respectively, the right and left Cauchy–Green tensors before the multiplicative decomposition.

Based on the assumption (19), Eq. (34) can be rewritten as [42]

$$\sigma = -p\mathbf{I} + 2\frac{\partial \Psi}{\partial I_1}\mathbf{B} + 2\frac{\partial \Psi}{\partial I_2}(I_1\mathbf{B} - \mathbf{B}^2) + 2\frac{\partial \Psi}{\partial I_4}\boldsymbol{a} \otimes \boldsymbol{a} + 2\frac{\partial \Psi}{\partial I_5}(\boldsymbol{a} \otimes \mathbf{B}\boldsymbol{a} + \boldsymbol{a}\mathbf{B} \otimes \boldsymbol{a}). \tag{35}$$

As I_2 and I_5 in (35) are not used in the materials under consideration, namely in the Neo–Hookean and GOH material models presented in Section 4, Eq. (35) can be reduced to

$$\sigma = -p\mathbf{I} + 2\frac{\partial \Psi}{\partial I_1}\mathbf{B} + 2\frac{\partial \Psi}{\partial I_4}\boldsymbol{a} \otimes \boldsymbol{a}. \tag{36}$$

p is not established directly from the deformation, but it can be obtained from the boundary conditions. Let us say that the elongation of the beam happens along one of the axes. Let us name it x (shown in Fig. 4). The components of stress tensors in other directions, i.e. y, z, are zero, and in that case, the expression for the deformation gradient tensor $\mathbf{F}$ is:

$$\mathbf{F} = \begin{bmatrix} \gamma & 0 & 0 \\ 0 & \frac{1}{\sqrt{\gamma}} & 0 \\ 0 & 0 & \frac{1}{\sqrt{\gamma}} \end{bmatrix}$$

From this condition, the form of p can be derived and then substituted into σ_{xx}. The final expression for tensile force can be written as

$$N = \int_0^h \int_0^w \sigma_{xx} dy dz = \int_0^H \int_0^W P_{xx} dy dz = P_{xx} HW, \tag{37}$$

where P_{xx} is a component of the first Piola–Kirchhoff stress tensor, $\mathbf{P} = J\sigma \cdot \mathbf{F}^{-T}$. γ, as a part of the deformation gradient tensor, is included in the expressions of stress tensors σ and $\mathbf{P}$. Then, after obtaining γ from (37), the final results for the displacements along the axis x will take the following form:
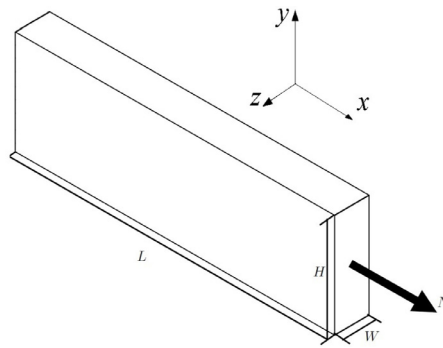
$$u_x = (\gamma - 1)L. \tag{38}$$

Fig. 4. Tensile loading case for ANCF- and ANSYS-based models.

Thus, we can conclude that the final result depends on the applied load, initial length, material properties, and initial cross-section area.

6.2. Analytical solutions for sub-tendon models

The analytical solutions for beams with arbitrary cross-sections are not straightforward, as in Section 6.1. To address it, we will rely on the approach derived in Section 5. Then, combining formulas (37) and (32), the final analytical solution takes the following form:

$$N = \sum_{\lambda \in \Lambda_{2n-1}} w_\lambda P_{xx}. \tag{39}$$

7. Numerical examples

In this section, numerical examples are solved to demonstrate the potential of the ANCF-based approach in comparison to the standard commercial software in the simple loading case for the straight and pre-twisted constructions, as well as Green's integration-based method in the description of the continuum-based ANCF beam element (denoted by ANCF using Green's integration). Firstly, we consider beams with rectangular cross-sections in which another end is simply supported, e.g. $r|_{x=0} = 0$ (to make a valid comparison with analytical solutions) and a tensile load is applied to the other end (in N), as presented in Fig. 4.

Secondly, for the verification of the whole procedure, the beam elongations of the rectangular cross-sections approximated via the Gauss-Green integration scheme under axial loading are analyzed and compared with the results obtained earlier. Then, we consider the beams with cross-sections of the human sub-tendons arising from the soleus muscle.

The results for the ANCF-based models will be compared with the presented analytical solutions and the results obtained by the commercial finite element software ANSYS. For the comparison, in ANSYS software, the 20-node brick element SOLID186 is used. The reason for the usage of the solid element instead of a beam one is the inability of the latter to capture transversal cross-section deformations. Furthermore, to avoid distortions at the edges of the ANSYS-based model and to make the solutions provided by the two approaches more comparable, in the geometrical center of the free end surface, we create the mass point MASS21, which is assumed to be a node. With this point, we couple the nodes' displacements on the free end's surface along the load direction. The load will be applied on the point.

This section will also present the convergence analysis. Considering a different number of nodes and nodal position coordinates in elements, the total number of DOFs is used in the analysis for comparison. The relative error is defined as

$$\text{Relative error} = \frac{||sol_{i+1} - sol_i||}{sol_{i+1}}, \tag{40}$$

where $|| \cdot ||$ is defined as L_2 norm. The relative error figures will be also accompanied by sets of parallel lines with different rates of convergence, i.e., $\frac{\text{Relative error}}{|DOFs-c|} = a$, where a is the rate of convergence, c is a positive constant, meaning the parallel shift of lines from the set along the abscissa.

7.1. Rectangular cross-section beam

Here, we consider the isotropic Neo–Hookean material model, with the constants for the strain energy density function taken from the earlier work of Obrezkov et al. [17], $c_{10} = 0.9$ MPa. To describe the rectangular cross-section, we take beams which have the width $W = 0.1$ m, the height $H = 0.1$ m, and the length $L = 1$ m. Firstly, we consider the straight beam. Results for the displacements are presented in Table 4.

Table 4
Comparison of the elongation test results in meter for the straight and pre-twisted beams from the Neo–Hookean material model.

Load [N]	Elongation [m]				
	Straight beam			Pre-twisted beam	
	Analytical	ANSYS	ANCF	ANSYS	ANCF
500	0.018866	0.018865	0.018866	0.018906	0.018866
2000	0.079830	0.079830	0.079831	0.079987	0.079832
3500	0.147857	0.147858	0.147861	0.148124	0.147861
5000	0.223538	0.223538	0.223543	0.223910	0.223543
8000	0.399475	0.399475	0.399487	0.400052	0.399487
9500	0.500000	0.500000	0.500017	0.500678	0.500017
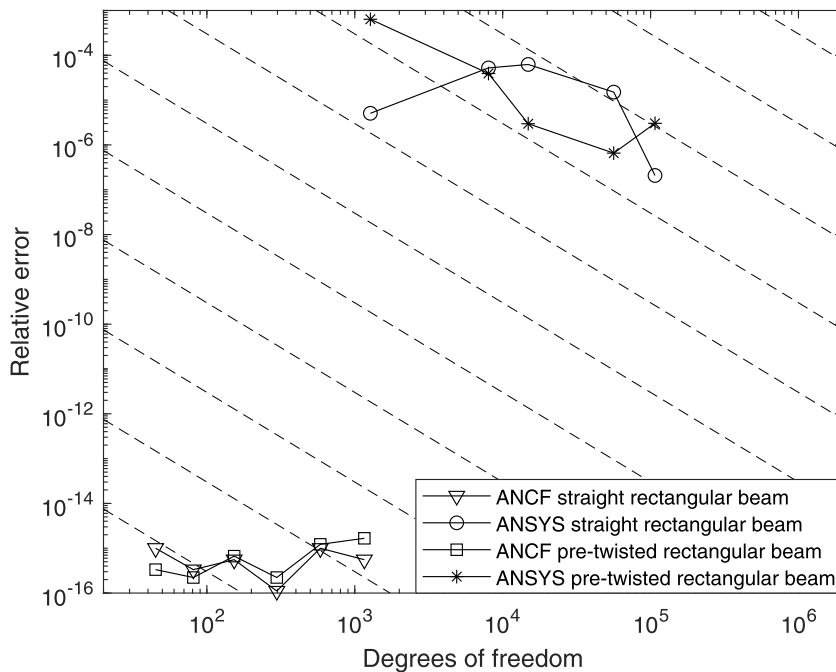
Fig. 5. Relative errors derived from Table 5 for the straight and pre-twisted beams from the Neo–Hookean material model subjected to $N = 9.5$ kN tensile force, dashed lines represent the rate of convergence equal to 2.

As one can see, the results are well-matched, but the ANCF-based model results are closer to the analytical ones. The maximal error for the ANSYS-based model is 0.005% and for the ANCF-based model 0.003%. Further, we compare the convergence rates for two models via the number of used degrees of freedom against the elongation results.

We can see from Fig. 5 that in the simple tensile test, the ANCF shows a better convergence rate than the solid element. The ANCF results are not presented in Table 5, because the differences between values obtained with the ANCF-based model are very small and have differences only in the 10th digit. Moreover, it was revealed that even one element with 27 DOFs is enough to obtain results very close to the analytical solutions.

The aim of the current paper is to propose an approach for sub-tendon's cross-section description in the framework of the absolute nodal coordinate formulation. There are many studies which provide information related to the pre-twisted sub-tendon structure [4–6,54]. Let us take a look at the deformation of the pre-twisted beam with the same physical and geometrical features. The only difference is that its cross-sections are twisted about the centroidal axis from 0° at the clamped end to ψ degrees at the free end. The centroidal axis of the beam remains straight. It is a worth mentioning that there are several kinds of the pre-twisted structures [55]. In this work, we consider only the linearly pre-twisted structure; see an example of the pre-twist in Fig. 6. As described in Section 6, an analytical solution for pre-twisted structures is not straightforward. It requires separate careful study especially in the case of hyperelastic anisotropic material models. Therefore, the analytical solution has not been included in this work. Instead, a solution provided by commercial finite element packages is offered as a reference solution.

Table 5
Elongation results for a number of mesh refinements for the straight and pre-twisted beams from the Neo–Hookean material model subjected to $N = 9.5$ kN tensile force in meter.

Elongation [m]		
ANSYS		
DOFs	Straight	Pre-twisted
243	0.49999	0.501355
1275	0.49999	0.500718
8019	0.50005	0.500679
14,883	0.49998	0.500682
56,355	0.49999	0.500681
107,163	0.50000	0.500678
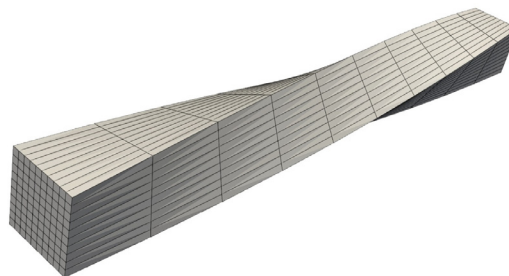
Fig. 6. Pre-twisted beam with $\psi = 90°$ in the initial configuration.

Table 6
Comparison of the elongation test results in meter for the straight and pre-twisted beams from the GOH material model.

Load [N]	Elongation [m]				
	Straight beam			Pre-twisted beam	
	Analytical	ANSYS	ANCF	ANSYS	ANCF
500	0.003246	0.003245	0.003246	0.003481	0.004548
2000	0.012743	0.012743	0.012744	0.013637	0.014701
3500	0.021792	0.021792	0.021794	0.023289	0.023870
5000	0.030316	0.030316	0.030320	0.032351	0.032457
8000	0.045675	0.045674	0.045679	0.048591	0.047902
9500	0.052526	0.052526	0.052532	0.055795	0.054800

As shown by Table 4, we have the same situation as in the previous numerical. The results given by ANSYS and ANCF are quite close to each other. Further, we again compare the convergence rates of the two solutions using graphical (Fig. 5) approach.

As shown before, the ANCF-based model for a pre-twisted structure has a faster convergence rate in comparison to the ANSYS-based model.

Now we consider a beam-type structure described with a so-called GOH material model (28). The beam has the following dimensions: the width $W = 0.1$ m, the height $H = 0.1$ m, and the length $L = 1$ m. The parameters used in this work are taken from the work of Khayyerin et al. [12] and are $c_{10} = 30.6$ kPa, $c_1 = 378.59$ kPa, $c_2 = 7.8085$, $a_0 = [0, 0, 1]^T$. The results for the tensile tests of the straight beams are presented in Table 6.

Table 6 shows the close results for ANCF- and ANSYS-based models, with the ANSYS model being closer to the analytical solution. Again, let us also compare the convergence rates for two models.

The results in Fig. 7 show a faster rate of convergence for the ANCF-based model than for the ANSYS-based one, and its results for the straight beam are not given in Table 7, because there are only value differences in the 13th digit. Then, we consider the deformations of the pre-twisted beams from the GOH material model. The geometrical and physical parameters are the same as in the previous example. The pre-twisted angle $\psi = 90°$ (see Fig. 6).

Table 6 shows the agreement between the solutions based on the ANCF and ANSYS approaches. Analogous to the previous examples, the solution convergence analysis demonstrates the performance and computational merits of the ANCF-based approach in the case of tensile deformation of the anisotropic materials.
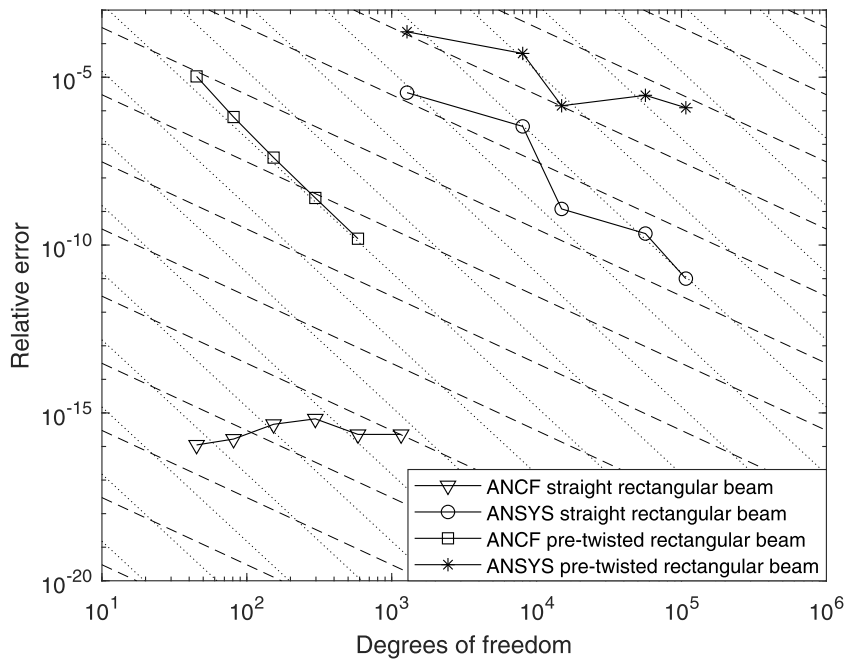
Fig. 7. Relative errors derived from Table 7 for the straight beams from the GOH material model subjected to $N = 9.5$ kN tensile force, dashed and dotted lines represent the rates of convergence equal to 2 and 4, respectively.

Table 7
Elongation results for a number of mesh refinements for the straight and pre-twisted beams from the GOH material model subjected to $N = 9.5$ kN tensile force in meter.

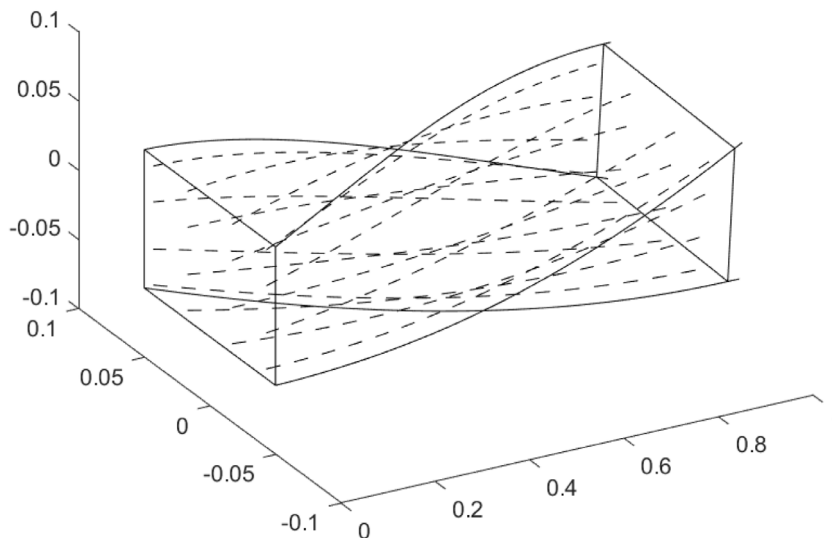| Elongation [m]				
ANSYS			ANCF	
DOFs	Straight	Pre-twisted	DOFs	Pre-twisted
243	0.052530	0.055963	27	0.0547885
1275	0.052526	0.055738	45	0.0547991
8019	0.052526	0.055789	81	0.0547997
14,883	0.052526	0.055790	153	0.0547998
56,355	0.052526	0.055793	297	0.0547998
107,163	0.052526	0.055795	585	0.0547998

Fig. 8. Fibers form for the pre-twisted beam, dashes are enlarged $\boldsymbol{a}_0$.
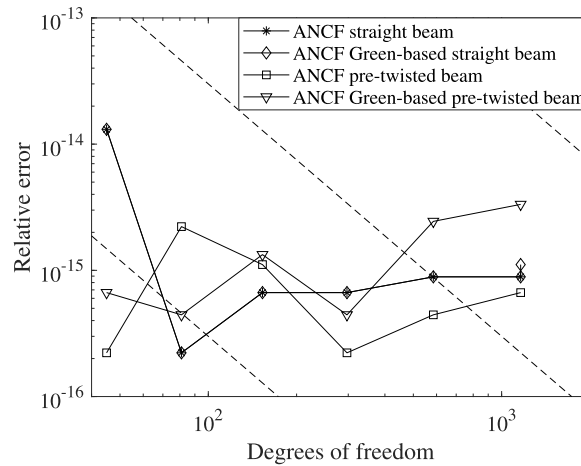
Fig. 9. Relative errors for the rectangular ANCF-based beams from the Neo–Hookean material model with standard Gaussian quadrature and Green's integration scheme subjected to $N = 9.5$ kN tensile force, dashed lines represent the rate of convergence equal to 2.
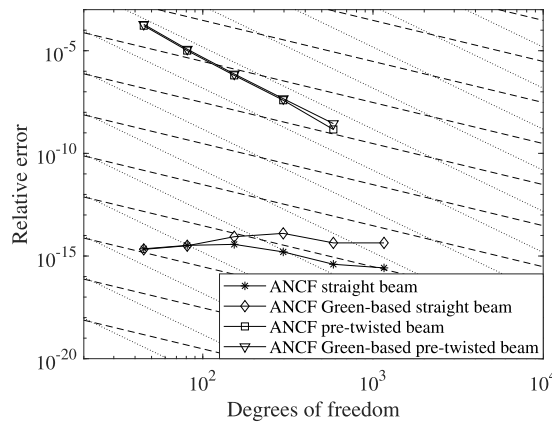

Fig. 10. Relative errors for the rectangular ANCF-based beams from the GOH material model with standard Gaussian quadrature and Green's integration scheme subjected to $N = 9.5$ kN tensile force, dashed and dotted lines represent the rates of convergence equal to 2 and 4, respectively.

The comparison between the results in Table 7 and Fig. 7 as well as the other previous graphical and tabular results presented in this section show that the ANCF-based model provides reliable results for the tensile tests for the beams from the hyperelastic materials with requirements of fewer degrees of freedom to obtain the solutions.

7.2. Rectangular cross-section beam via Gauss–Green integration scheme

Let us again consider the beams with a rectangular cross-section with $W = 0.1$ m, $H = 0.1$ m, and $L = 1$ m. Firstly, to compare the results with Section 7, we take the Neo–Hookean and GOH material models, with the material constants related to these models. Results for the tests of straight and pre-twisted beams are very close, with the same convergence rate for the straight beam and approximately the same for the pre-twisted ones (see Figs. 9 and 10).

Table 8, Figs. 9 and 10 show that for the simplest cross-section (rectangular), the Green-based integration formula agrees well with the standard Gaussian quadrature integration scheme. The model based on the Gauss-Green cubature formula provides similar results, with approximately the same convergence rate. Thus, one can conclude that the developed element based on Green's integration scheme is a reliable substitution for the ANCF with the standard Gaussian quadrature integration scheme in tensile deformations. The results for the Neo–Hookean model are not given in tabular form, as the relative error is small, with its maximum at about 10^{-9}.

7.3. The Achilles sub-tendon cross-sections

It was already mentioned that previous studies have mostly considered the Achilles tendons as one-piece constructions with simple cross-sections. However, the tendons are a combination of three interconnected sub-tendons with arbitrary cross-sections [4–6,54]. Each of the sub-tendons has a complicated shape. To demonstrate the usability of the developed

Table 8
Comparison of the elongation test results of the ANCF-based beams from the GOH material model with standard Gaussian quadrature and Green's integration schemes

Load [N]	Elongation [m] of the ANCF-based beams			
	Using Green's integration		Standard integration scheme	
	$\psi = 0°$	$\psi = 90°$	$\psi = 0°$	$\psi = 90°$
500	0.003248	0.004445	0.003248	0.004548
2000	0.012754	0.014474	0.012754	0.014701
3500	0.021813	0.023627	0.021813	0.023870
5000	0.030346	0.032207	0.030346	0.032457
8000	0.045725	0.047646	0.045725	0.047902
9500	0.052587	0.054529	0.052587	0.054800
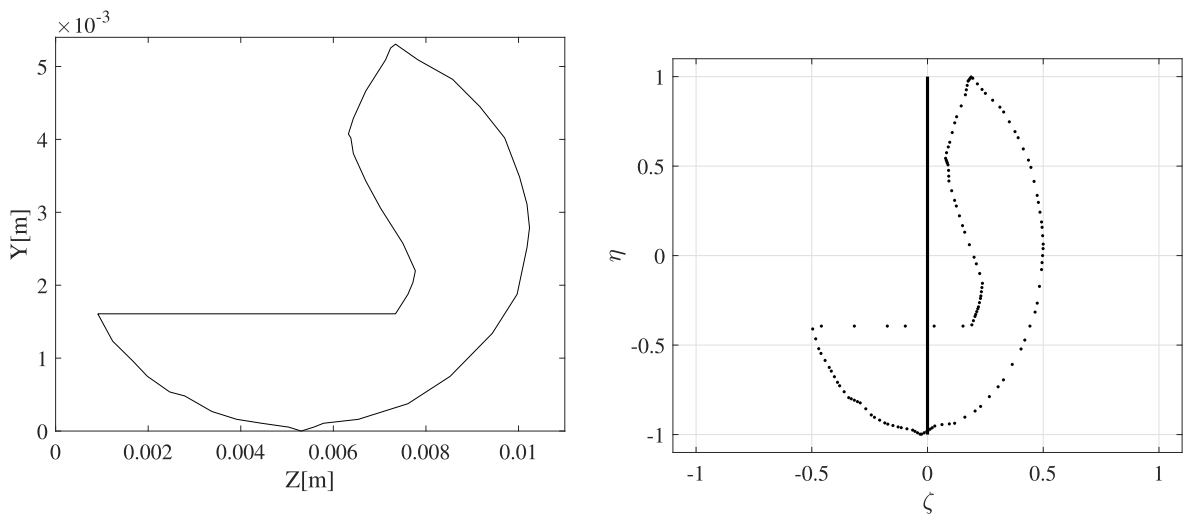
(a) Geometry approximation of the sub-tendon arising from the soleus muscle

(b) Integration approximation by the Gauss-Green cubature formula

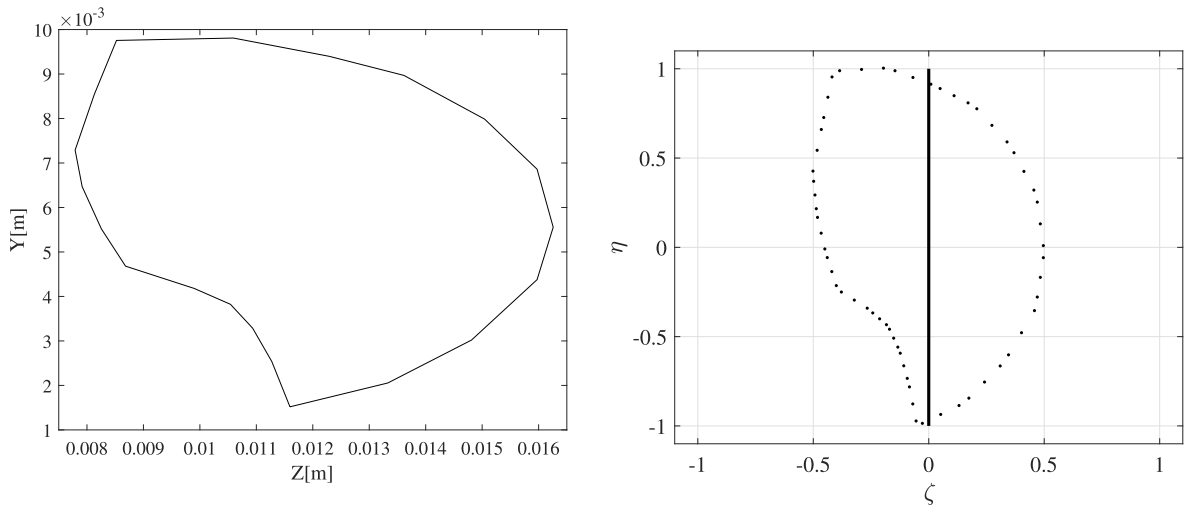**Fig. 11.** The sub-tendon representation for the Type I tendon [6].

continuum-based ANCF beam element with the arbitrary cross-sectional description, the Achilles sub-tendons under elongation are used as numerical examples. There are three types of the Achilles tendon [5]. In this work, we consider two of the most common ones: Type I and Type II [6]. In our numerical analyses, we extract the geometrical description of sub-tendons that are connected to the soleus muscle.

Now we deal with the first type of the Achilles tendon. The exact geometrical data of the sub-tendon are not presented in Edama et al. [6]. Therefore, we resorted to a CAD software to approximate the points' positions. The coordinates for the leftmost point are $(17, 30)$. For the rightmost, the highest and the lowest points, the coordinates are, respectively, $(191, 52)$, $(137, 99)$ and $(99, 0)$. Based on the geometrical results of Yin et al. [50] related to this tendon type, we can obtain the approximation area of 19.2 mm^2 and the length of $L = 0.04$ m. The Type I sub-tendon's cross-section representation can be seen in Fig. 11(a) alongside its point approximation in Fig. 11(b).

Then, we consider the Type II tendon. The tendon length is $L = 0.07$ m according to Yin et al. [50]. Again, resorting to CAD software, the approximate position for the leftmost point is $(438, 436)$, and $(910, 311)$, $(593, 549)$, and $(649, 85)$ for the rightmost, the highest and the lowest points, respectively. The sub-tendon cross-sectional area equals 47.135 mm^2, which can be seen in Fig. 12(a) and its approximation at the integration point form is given in Fig. 12(b).

Due to the usage of the graphical editor, there is discretization error. For the Type I tendon, it is about 0.36 % and for the Type II tendon 0.14 %.

Moreover, the sub-tendons are the pre-twisted structure [4,5,54]. Here, we consider the straight and pre-twisted beams (see Fig. 13(a) and (b), for the Type I sub-tendon, and Fig. 14(a) and (b), for Type II).
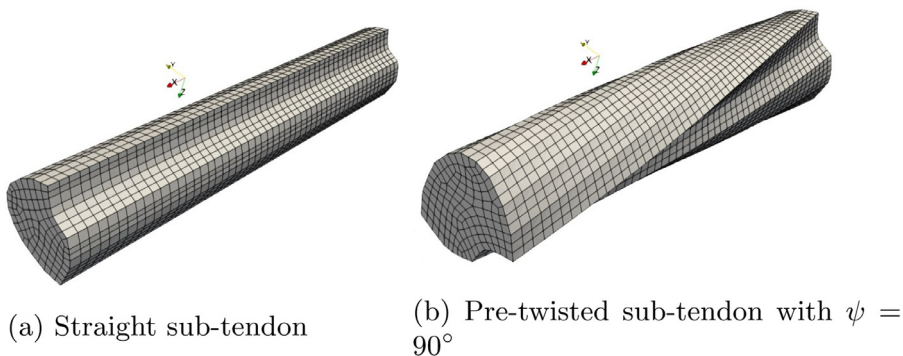
(a) Geometry approximation of the sub-tendon arising from the soleus muscle

(b) Integration approximation by the Gauss-Green cubature formula

Fig. 12. The sub-tendon representation for the Type II tendon.
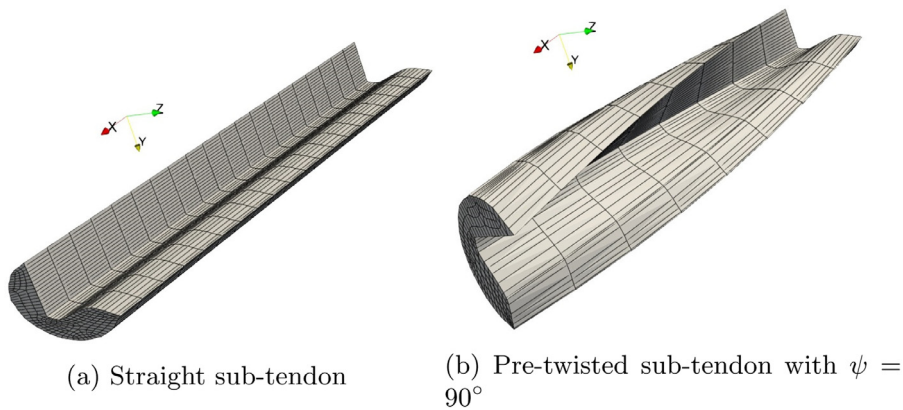
(a) Straight sub-tendon

(b) Pre-twisted sub-tendon with $\psi = 90°$

Fig. 13. The sub-tendon representations of the Type I tendon.

(a) Straight sub-tendon

(b) Pre-twisted sub-tendon with $\psi = 90°$

Fig. 14. The sub-tendon representations of the Type II tendon.

Table 9

Comparison of the elongation test results in [mm] for the straight and pre-twisted sub-tendons Type I and Type II from the Neo–Hookean material model .

Elongation [mm] of the straight sub-tendons						
Load [N]	Sub-tendon Type I			Sub-tendon Type II		
	Analytical	ANSYS	ANCF	Analytical	ANSYS	ANCF
10	0.067470	0.067637	0.068295	0.048048	0.048047	0.048098
20	0.135167	0.135503	0.136798	0.096161	0.961606	0.096262
30	0.203092	0.203599	0.205511	0.144341	0.144340	0.144492
40	0.192587	0.271925	0.274436	0.192587	0.192585	0.192788
50	0.240899	0.340481	0.343575	0.240899	0.240897	0.241149
60	0.408247	0.409270	0.412929	0.289277	0.289275	0.289577
70	0.477093	0.478291	0.482499	0.337722	0.337719	0.338070
80	0.546172	0.547548	0.552288	0.386233	0.386230	0.386630
90	0.615484	0.617034	0.622297	0.434811	0.434808	0.435256
100	0.685030	0.686759	0.692528	0.483456	0.483452	0.483949
Elongation [mm] of the pre-twisted sub-tendons						
Load [N]	Sub-tendon Type I			Sub-tendon Type II		
	ANSYS	ABAQUS	ANCF	ANSYS	ANCF	
10	0.079618	0.074342	0.068297	0.048047	0.048098	
20	0.157767	0.147273	0.136805	0.961606	0.096262	
30	0.234953	0.219354	0.205526	0.144340	0.144492	
40	0.311484	0.290901	0.274462	0.192585	0.192788	
50	0.387556	0.362131	0.343614	0.240897	0.241150	
60	0.463306	0.433186	0.412984	0.289275	0.289578	
70	0.538829	0.504157	0.482574	0.337719	0.338072	
80	0.614198	0.575105	0.552385	0.386230	0.386632	
90	0.689465	0.646091	0.622417	0.434809	0.435259	
100	0.764674	0.717157	0.692674	0.483452	0.483952	

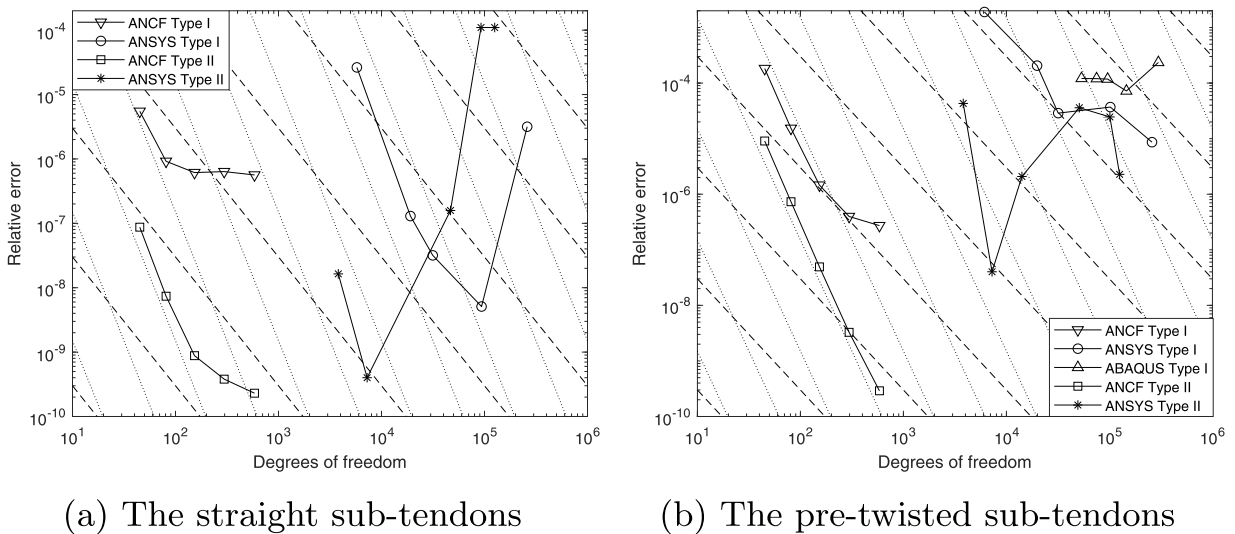(a) The straight sub-tendons　　　(b) The pre-twisted sub-tendons

Fig. 15. Relative errors derived from Table 10 for the sub-tendons of Type I and Type II from the Neo–Hookean material model subjected to $N = 100$ N tensile force, dashed and dotted lines represent the rates of convergence equal to 2 and 4, respectively.

7.3.1. Neo–Hookean material model

In this subsection, we repeat the tensile example presented in Yin et al. [50]. We use the Neo–Hookean material model with the shear modulus equal to $c_{10} = 103.1$ MPa undergoing the maximum applied tensile load of 100 N.

As one can see from Table 9, the results are in a good agreement for the straight structures. For Type I, the ANSYS-based model provides results, where the difference between analytical solutions is about 0.3%. The difference between the ANCF-based model and analytical solutions is about 1.1%. In the Type II model, the differences are 0.001% in the ANSYS-based model and 0.1% in the ANCF-based model. Further, we compare the converge rates for the two models (see Fig. 15(a) and (b).

Table 10

Elongation results for a number of mesh refinements for the straight and pre-twisted sub-tendons from the Neo–Hookean material model subjected to $N = 100$ N tensile force in [mm].

Elongation [mm] of the straight sub-tendons							
ANCF			ANSYS				
DOFs	Type I	Type II	DOFs	Type I		DOFs	Type II
27	0.692520	0.4839487	2895	0.686781		2331	0.4834519
45	0.692525	0.4839488	5766	0.686755		3807	0.4834519
81	0.692526	0.4839488	19,107	0.686755		7251	0.4834519
153	0.692527	0.4839488	31,443	0.686755		46,749	0.4834520
297	0.692527	0.4839488	93,618	0.686755		92,529	0.4835619
585	0.692528	0.4839488	259,641	0.686759		125,568	0.4834520
Elongation [mm] of the pre-twisted sub-tendons							
ANCF			ANSYS				ABAQUS
DOFs	Type I	Type II	DOFs	Type I	DOFs	Type II	DOFs	Type I
27	0.69247	0.48394	2898	0.766294	2331	0.4834518	47,292	0.7165
45	0.69265	0.48395	6123	0.764394	3807	0.4834518	53,556	0.7166
81	0.69267	0.48395	19,842	0.764600	7251	0.4834519	75,042	0.7167
153	0.69267	0.48395	31,830	0.764629	46,749	0.4834520	96,132	0.7168
297	0.69267	0.48395	102,063	0.764666	92,529	0.4835619	146,145	0.7169
585	0.69267	0.48395	259,074	0.764674	125,568	0.4834520	298,815	0.7172

It is obvious that the ANCF-based models require significantly fewer DOFs for the structures' descriptions, and can deliver accurate results with the discretization of one element. Now, we consider the deformation of the pre-twisted models. There are several proposals related to the pre-twisting Handsfield et al. [4], Pękala et al. [54]. In this work, we consider $\psi = 90°$.

A comparison of the elongation results in Table 9 indicates that the results of the two models of the Type I sub-tendon differ significantly in the case of the pre-twisted structures. The ANSYS-based model gives noticeably higher displacements for the body with the complicated cross-section. Meanwhile, the model based on the ANCF approach shows almost the same results as the straight beam, with a small difference up to 1.1% for the maximal displacement. Due to the significant discrepancy between the ANCF and ANSYS solutions for the maximum elongation, the tensile test was replicated with another software, namely, ABAQUS, using the quadratic 20-node continuum element in ABAQUS denoted as C3D20, which is similar to the used ANSYS element type. According to Table 9, the ABAQUS solutions for the elongation are closer to the ANCF results than the ANSYS solution. Further, we consider the Type II sub-tendon (see Table 9).

For both pre-twisted models, the rate of convergence of solutions are presented in Fig. 15(b), Table 10.

7.3.2. GOH material model

As mentioned above, the real biological tissues are anisotropic. To simulate such behaviour, we consider the GOH material model (28) with the material parameters adopted from Section 7.1 and by applying a tensile load of up to 100. We also consider the straight and pre-twisted beam models. Let us firstly, consider the Type I sub-tendon, with the total area of 19.15 mm^2, the length of $L = 0.04$ m [50], and the material parameters $c_{10} = 30.6$ kPa, $c_1 = 378.59$ kPa, $c_2 = 7.8085$, $a_0 = [0, 0, 1]^T$ [12].

Table 11 demonstrates that the results are relatively close to each other for the straight sub-tendons. The differences of the analytical solutions are about 0.14% for ANCF and 0.1% for ANSYS. Further, Fig. 16(a) and Table 12 display the convergence rates for both models of the sub-tendons.

Now we consider a pre-twisted tendon. Section 7.3.1 and Table 9 showed for the Type I sub-tendon that the ANCF delivers results close to the analytical results in the case of a straight beam and ABAQUS solutions in the case of a pre-twisted structure. Therefore, for this type, we consider only one ANCF-based model. In the case of the Type II sub-tendon, we provide our readers with both models.

Comparing the results of Table 11, the pre-twisted anisotropic beam underwent greater elongations under an uniaxial load than the straight beam, which can be partly explained by the structure's longer fibers (see Fig. 8). As one can notice, the difference between the results of the ANCF- and ANSYS-based models is quite small, despite the complicated form and sophisticated structure. The comparison of the rate of convergence for that case is presented in Fig. 16(b). Fig. 16(b) shows that the pre-twisted sub-tendon, regardless of its type, could be described with relatively high accuracy with one ANCF-based element only.

8. Limitations

This research has several limitations. In the study, the geometrical data were extracted with the usage of the graphical redactor, therefore, the accuracy is questionable. To mitigate this limitation, the error estimation due to discretization errors is presented. Additionally, the cross-section area is considered the same along the longitudinal axis. However, it can vary, but there is no data to approximate such geometry. The interaction between fluid and solid is also omitted from this work.

Table 11

Comparison of the elongation test results in [mm] for the straight and pre-twisted sub-tendons Type I and Type II from the GOH material model .

Elongation [mm] of the straight sub-tendons					
Load [N]	Sub-tendon Type I			Sub-tendon Type II		
	Analytical	ANSYS	ANCF	Analytical	ANSYS	ANCF
10	1.25805	1.2627115	1.25523	0.94460	0.944630	0.94334
20	2.25806	2.2626906	2.25444	1.82587	1.825854	1.82358
30	3.02459	3.0299230	3.02145	2.63080	2.630783	2.62774
40	3.62189	3.6274931	3.61986	3.35677	3.356751	3.35318
50	4.10099	4.1066824	4.10039	4.00787	4.007843	4.00393
60	4.49603	4.5017274	4.49700	4.59139	4.591365	4.58726
70	4.82943	4.8351068	4.83208	5.11556	5.115528	5.11134
80	5.11627	5.1219006	5.12065	5.58826	5.588231	5.58403
90	5.36697	5.3725359	5.37312	6.01657	6.016543	6.01239
100	5.58893	5.5944432	5.59685	6.40660	6.406570	6.40251
Elongation [mm] of the pre-twisted sub-tendons					
Load [N]	Sub-tendon Type I		Sub-tendon Type II		
	ANCF		ANSYS	ANCF	
10	1.490723		1.022816	1.077669	
20	2.506607		1.976414	1.978382	
30	3.283207		2.840383	2.799663	
40	3.887926		3.615008	3.541619	
50	4.373086		4.305867	4.208678	
60	4.773447		4.920263	4.808188	
70	5.111770		5.473186	5.348351	
80	5.403297		5.968654	5.837045	
90	5.658558		6.416557	6.281320	
100	5.885057		6.823999	6.687249	

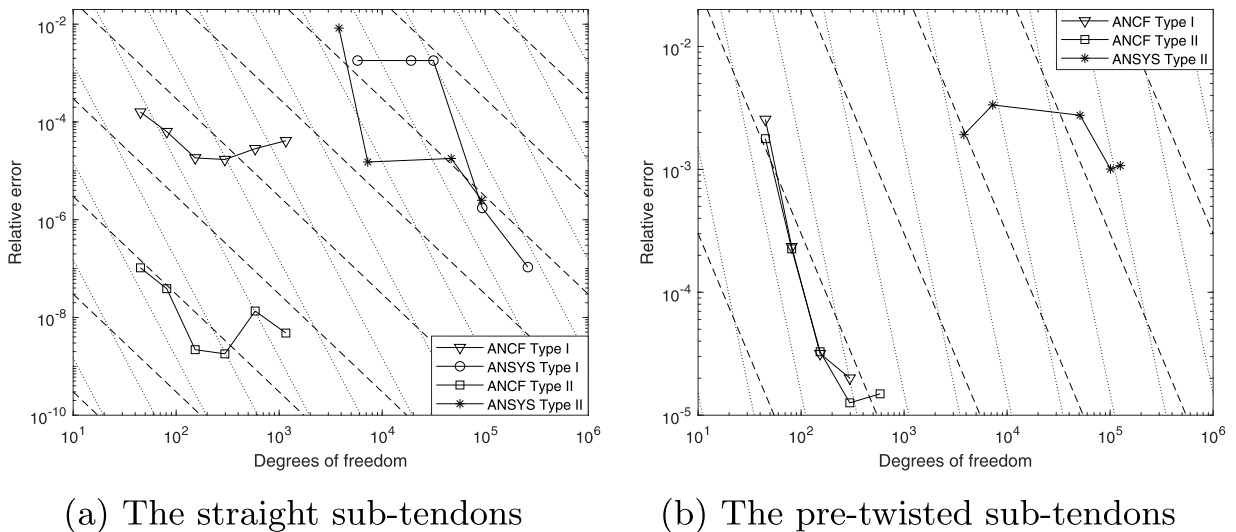(a) The straight sub-tendons   (b) The pre-twisted sub-tendons

Fig. 16. Relative errors derived from Table 11 for the sub-tendons of Type I and Type II from the GOH material model subjected to $N = 100$ N tensile force, dashed and dotted lines represent the rates of convergence equal to 2 and 4, respectively.

Nonetheless, it can be added with the usage of poroelasticity as it is done for the rat Achilles tendons in Khayyerin et al. [12], Khayyeri et al. [56]. The material time-dependency is not included, however, the compatibility of the ANCF element and viscoelastic models was successfully considered in Obrezkov et al. [21]. Additionally, the current research aims to provide a tool for the description of beam-like structures, and such an important issue as uncertainties of parameters of the models is not considered here. Even with the limitations imposed on the geometry and physical parameters, it is shown, that the elongation results for the pre-twisted sub-tendon Type I differ for ABAQUS-, ANCF- and ANSYS-based models, although the two first are close to each other. Moreover, the material model used in this study could be still approximated to be closer to the real tendon's tissues. In our study, the fibers of the anisotropic model follow the pre-twist angle given for the whole model. However, there are studies, as [54], that show fiber pre-twist for the sub-tendons can differ from the pre-twist of

Table 12

Elongation results for a number of mesh refinements for the straight and pre-twisted sub-tendons Type I and Type II from the GOH material model subjected to $N = 100$ N tensile force in [mm].

Elongation [mm] of the straight sub-tendons						
ANCF			ANSYS		ANSYS	
DOFs	Type I	Type II	DOFs	Type I	DOFs	Type II
27	5.59689	6.40251	2895	5.596247	2331	6.414917
45	5.59691	6.40251	5766	5.594443	3807	6.406605
81	5.59692	6.40251	19,107	5.596247	7251	6.406590
153	5.59692	6.40251	31,443	5.594445	46,749	6.406572
297	5.59693	6.40251	93,618	5.594443	92,529	6.406570
585	5.59690	6.40251	259,644	5.594443	125,568	6.406570
Elongation [mm] of the pre-twisted sub-tendons						
ANCF					ANSYS	
DOFs	Type I		Type II		DOFs	Type II
27	5.882218		6.685200		3807	6.817963
45	5.884770		6.686978		7251	6.821308
81	5.885005		6.687203		51,039	6.824065
153	5.885005		6.687236		101,019	6.825072
297	5.885057		6.687249		125,568	6.823999

the model. Another important feature of the biological tissue, presence of the inner stresses can be added into the model via inclusion of the pre-strain field [57].

9. Conclusion

This work applies the continuum-based ANCF beam element to analyze the deformation of the human Achilles sub-tendons under tensile loading. To describe the sub-tendons, a continuum-based ANCF beam element with an arbitrary cross-section description has been developed based on the Gauss-Green cubature integration formula. The developed element is verified analytically and numerically with commercial finite element software using three-dimensional continuum elements. The material parameters were taken from the works of other researchers. It was found that the developed ANCF element with an arbitrary cross-section description performed well in all numerical tests. Furthermore, the computational advantage of the proposed ANCF-based approach for the deformation analysis of the Achilles sub-tendon in terms of the convergence rate against commercial software was demonstrated. Moreover, it was found that if the sub-tendons are pre-twisted, the ANCF-based beam model provides more reliable solutions than commercial finite element software does. It can be concluded that the developed ANCF elements with an arbitrary cross-section description based on the Gauss-Green integration scheme is a reliable and computationally efficient approach for analyzing the deformation of Achilles sub-tendons. The developed element has potential also in other applications with beam-like flexible structures, such as in the modelling of soft robotics, where flexible beam-like structures often appear and can now be described in more realistic forms.

Declaration of Competing Interest

The authors declare that they have no known competing financial interests or personal relationships that could have appeared to influence the work reported in this paper.

Appendix A. Cross-sectional deformation

The continuum-based ANCF beam are able to capture the cross-section deformations due to their kinematic description given in Section 2. To demonstrate it, the results of the deformed cross-section areas at the applied force end are gathered in Table A.13. To obtain the values of the deformed ANSYS-based model due to the absence of the procedure in the software postprocessor the following procedure has been done: the software was put into the preprocessor again; using saved nodal positions the form was generated with SURF154 surface skin elements; the recreated area was calculated with the preprocessor command.

As one can see from Table A.13, the results for the tendon Type II and rectangular cross-sections are in good agreement. However, the results of the ANSYS-based model for the Type I tendon are significantly different from the analytical and

Table A1

Cross-sectional areas before and after deformation in $[\text{mm}^2]$.

Cross-sectional areas $[\text{mm}^2]$				Area after deformation		
Cross-section type	Material model	Pre-twist angle	Area before deformation	Analytical solution	ANSYS solution	ANCF solution
Rectangular	Neo–Hookean	$\psi = 0°$	10^4	6.667×10^3	6.667×10^3	6.667×10^3
Rectangular	Neo–Hookean	$\psi = 90°$	10^4	–	6.667×10^3	6.667×10^3
Rectangular	GOH	$\psi = 0°$	10^4	9.5×10^3	9.501×10^3	9.501×10^3
Rectangular	GOH	$\psi = 90°$	10^4	–	9.5142×10^3	9.482×10^3
Type I	Neo–Hookean	$\psi = 0°$	19.15	18.877	20.957	18.949
Type I	Neo–Hookean	$\psi = 90°$	19.15	–	21.009	18.949
Type I	GOH	$\psi = 0°$	19.15	16.849	19.564	16.909
Type I	GOH	$\psi = 90°$	19.15	–	–	16.224
Type II	Neo–Hookean	$\psi = 0°$	47.135	46.812	46.121	46.884
Type II	Neo–Hookean	$\psi = 90°$	47.135	–	46.125	46.884
Type II	GOH	$\psi = 0°$	47.135	43.183	43.161	43.252
Type II	GOH	$\psi = 90°$	47.135	–	43.357	41.695

ANCF-based solutions. That indicates the limited ability of the commercial software to reproduce this sophisticated tendon form.

References

[1] T. Finni, P.V. Komi, Two methods for estimating tendinous tissue elongation during human movement, J. Appl. Biomech. 18 (2002) 180–188, doi:10.1123/jab.18.2.180.

[2] J.H.-C. Wang, Q. Guo, B. Li, Tendon biomechanics and mechanobiology—A minireview of basic concepts and recent advancements, J. Hand Ther. 25 (2) (2012) 133–141, doi:10.1016/j.jht.2011.07.004.

[3] G.G. Handsfield, J.M. Inouye, L.C. Slane, D.G. Thelen, G.W. Miller, S.S. Blemker, A 3D model of the Achilles tendon to determine the mechanisms underlying nonuniform tendon displacements, J. Biomech. 51 (2017) 17–25, doi:10.1016/j.jbiomech.2016.11.062.

[4] G.G. Handsfield, J. Greiner, J. Madlf, E.A. Rog-Zielinska, E. Hollville, B. Vanwanseele, V. Shim, Achilles subtendon structure and behavior as evidenced from tendon imaging and computational modeling, Front. Sports Act. Living 70 (2020) 1519–1538, doi:10.3389/fspor.2020.00070.

[5] T. Finni, M. Bernabei, G.C. Baan, W. Noort, C. Tijs, H. Maas, Non-uniform displacement and strain between the soleus and gastrocnemius subtendons of rat Achilles tendon, Scand. J. Med. Sci. Sports 28 (2018) 1009–1017, doi:10.1111/sms.13001.

[6] M. Edama, M. Kubo, H. Onishi, T. Takabayashi, T. Inai, E. Yokoyama, W. Hiroshi, N. Satoshi, I. Kageyama, The twisted structure of the human Achilles tendon, Scand. J. Med. Sci. Sports 25 (2015) e497–e503, doi:10.1111/sms.12342.

[7] W. Hansen, V.B. Shim, S. Obst, D.G. Lloyd, R. Newsham-West, R.S. Barrett, Achilles tendon stress is more sensitive to subject-specific geometry than subject-specific material properties: afinite element analysis, J. Biomech. 56 (2017) 26–31, doi:10.1016/j.jbiomech.2017.02.031.

[8] E. Morales-Orcajo, T.R. Souza, J. Bayod, E. Barbosa de LasCasas, Non-linear finite element model to assess the effect of tendon forces on the foot-ankle complex, Med. Eng. Phys. 49 (2017) 71–78, doi:10.1016/j.medengphy.2017.07.010.

[9] R.A. taş, D.O. Lucaciu, Finite element analysis of the Achilles tendon while running, Acta Med. Marisiensis 59 (2013) 8–11, doi:10.2478/amma-2013-0002.

[10] R. Kinugasa, N. Yamamura, S. Sinha, S. Takagi, Influence of intramuscular fiber orientation on the Achilles tendon curvature using three-dimensional finite element modeling of contracting skeletal muscle, J. Biomech. 49 (2016) 3592–3595, doi:10.1016/j.jbiomech.2016.09.014.

[11] V.B. Shim, W. Hansen, R. Newsham-West, L. Nuri, S. Obst, C. Pizzolato, D.G. Lloyd, R.S. Barrett, Influence of altered geometry and material properties on tissue stress distribution under load in tendinopathic Achilles tendons—A subject-specific finite element analysis, J. Biomech. 82 (2019) 142–148, doi:10.1016/j.jbiomech.2018.10.027.

[12] H. Khayyerin, G. Longo, A. Gustafsson, H. Isaksson, Comparison of structural anisotropic soft tissue models for simulating Achilles tendon tensile behaviour, J. Mech. Behav. Biomed. Mater. 61 (2016) 431–443, doi:10.1016/j.jmbbm.2016.04.007.

[13] A.A. Shabana, Definition of the slopes and the finite element absolute nodal coordinate formulation, Multibody Syst. Dyn. 1 (1997) 339–348, doi:10.1023/A:1009740800463.

[14] E. Grossi, A.A. Shabana, Analysis of high-frequency ANCF modes: Navier–Stokes physical damping and implicit numerical integration, Acta Mech. 230 (2019) 2581–2605, doi:10.1007/s00707-019-02409-8.

[15] K. Nachbagauer, State of the art of ANCF elements regarding geometric description, interpolation strategies, definition of elastic forces, validation and the locking phenomenon in comparison with proposed beam finite element, Arch. Comput. Methods Eng. 21 (2014) 293–319, doi:10.1007/S11831-014-9117-9.

[16] K. Nachbagauer, P. Gruber, J. Gerstmayr, A 3D shear deformable finite element based on the absolute nodal coordinate formulation, Multibody Dyn. 28 (2013) 77–96, doi:10.1007/978-94-007-5404-1_4.

[17] L.P. Obrezkov, M.K. Matikainen, A.B. Harish, A finite element for soft tissue deformation based on the absolute nodal coordinate formulation, Acta Mech. 231 (2020) 1519–1538, doi:10.1007/s00707-019-02607-4.

[18] A.A. Shabana, D. Zhang, ANCF curvature continuity: application to soft and fluid materials, Nonlinear Dyn. 100 (2020) 1497–1517, doi:10.1007/s11071-020-05550-5.

[19] J. Rhim, S.W. Lee, A vectorial approach to computational modelling of beams undergoing finite rotations, Int. J. Numer. Methods Eng. 41 (1998) 527–540, doi:10.1002/(SICI)1097-0207(19980215)41:3<527::AID-NME297>3.0.CO;2-7.

[20] H. Ebel, M.K. Matikainen, V.-V. Hurskainen, A. Mikkola, Higher-order beam elements based on the absolute nodal coordinate formulation for three-dimensional elasticity, Nonlinear Dyn. 88 (2017) 1075–1091, doi:10.1007/s11071-016-3296-x.

[21] L.P. Obrezkov, P. Eliasson, A.B. Harish, M.K. Matikainen, Usability of finite elements based on the absolute nodal coordinate formulation for the Achilles tendon modelling, Int. J. Non-Linear Mech. 129 (2021) 103662, doi:10.1016/j.ijnonlinmec.2020.103662.

[22] J. Gerstmayr, H. Sugiyama, A. Mikkola, Review on the absolute nodal coordinate formulation for large deformation analysis of multibody systems, J. Comput. Nonlinear Dyn. 8 (2013) 031016, doi:10.1115/1.4023487.

[23] M. Patel, A.A. Shabana, Locking alleviation in the large displacement analysis of beam elements: the strain split method, Acta Mech. 229 (2018) 2923–2946, doi:10.1007/s00707-018-2131-5.

[24] K. Kerkkänen, J. Sopanen, A. Mikkola, A linear beam finite element based on the absolute nodal coordinate formulation, J. Mech. Des. 127 (2005) 621–630, doi:10.1115/1.1897406.

[25] D. Garcìa-Vallejo, A.M. Mikkola, J.L. Escalona, A new locking-free shear deformable finite element based on absolute nodal coordinates, Nonlinear Dyn. 50 (2007) 249–264, doi:10.1007/s11071-006-9155-4.

[26] A. Shabana, R. Yakoub, Three dimensional absolute nodal coordinate formulation for beam elements: theory, J. Mech. Des. 123 (2001) 606–613, doi:10.1115/1.1410100.

[27] A.L. Schwab, J.P. Meijaard, Comparison of three-dimensional flexible beam elements for dynamic analysis: classical finite element formulation and absolut nodal coordinate formulation, J. Comput. Nonlinear Dyn. 5 (2010) 011010–1–011010–10, doi:10.1115/1.4000320.

[28] H. Sugiyama, J. Gerstmayr, A.A. Shabana, Deformation modes in the finite element absolute nodal coordinate formulation, J. Sound Vib. 298 (2006) 1129–1149, doi:10.1016/j.jsv.2006.06.037.

[29] M.K. Matikainen, O. Dmitrochenko, A. Mikkola, Beam elements with trapezoidal cross section deformation modes based on the absolute nodal coordinate formulation, AIP Conf. Proc. 1281 (1) (2010) 1266–1270, doi:10.1063/1.3497930.

[30] M. Matikainen, A. Valkeapää, A. Mikkola, A.L. Schwab, A study of moderately thick quadrilateral plate elements based on the absolute nodal coordinate formulation, Multibody Syst. Dyn. 31 (2014) 309–338, doi:10.1007/s11044-013-9383-6.

[31] Z. Shen, P. Li, C. Liu, G. Hu, A finite element beam model including cross-section distortion in the absolute nodal coordinate formulation, Nonlinear Dyn. 77 (3) (2014) 1019–1033, doi:10.1007/s11071-014-1360-y.

[32] B.Bozorgmehri, V.-V. Hurskainen, M.K. Matikainen, A. Mikkola, Dynamic analysis of rotating shafts using the absolute nodal coordinate formulation, J. Sound Vib. 453 (2019) 214–236, doi:10.1016/j.jsv.2019.03.022.

[33] G. Orzechowski, Analysis of beam elements of circular cross section using the absolute nodal coordinate formulation, Arch. Mech. Eng. 59 (2012) 283–296, doi:10.2478/v10180-012-0014-1.

[34] L.P. Obrezkov, A. Mikkola, M.K. Matikainen, Performance review of locking alleviation methods for continuum ANCF beam elements, Nonlinear Dyn. 109 (2022) 531–546, doi:10.1007/s11071-022-07518-z.

[35] G. He, M. Patel, A. Shabana, Integration of localized surface geometry in fully parameterized ANCF finite elements, Comput. Methods Appl. Mech. Eng. 313 (2017) 966–985, doi:10.1016/j.cma.2016.10.016.

[36] G. He, K. Gao, J. Jiang, R. Liu, Q. Li, Shape optimization of a flexible beam with a local shape feature based on ANCF, J. Adv. Mech. Des., Syst., Manuf. 13 (2019) JAMDSM0059, doi:10.1299/jamdsm.2019jamdsm0059.

[37] A. Sommariva, M. Vianello, Product Gauss cubature over polygons based on Greens integration formula, BIT Numer. Math. 47 (2007) 441–453, doi:10.1007/s10543-007-0131-2.

[38] A. Sommariva, M. Vianello, Gauss–Green cubature and moment computation over arbitrary geometries, J. Comput. Appl. Math. 231 (2009) 886–896, doi:10.1016/j.cam.2009.05.014.

[39] G. Chagnon, J. Ohayon, J.-L. Martiel, D. Favier, Chapter 1—Hyperelasticity modeling for incompressible passive biological tissues, in: Y. Payan, J. Ohayon (Eds.), Biomechanics of Living Organs, Translational Epigenetics, vol. 1, Academic Press, Oxford, 2017, pp. 3–30.

[40] M. Gilchrist, J. Murphy, W. Parnell, B. Pierrat, Modelling the slight compressibility of anisotropic soft tissue, Int. J. Solids Struct. 51 (2014) 3857–3865, doi:10.1016/j.ijsolstr.2014.06.018.

[41] G.A. Holzapfel, T.C. Gasser, A viscoelastic model for fiber-reinforced composites at finite strains: continuum basis, computational aspects and applications, Comput. Methods Appl. Mech. Eng. 190 (2001) 4379–4403, doi:10.1016/S0045-7825(00)00323-6.

[42] G.A. Holzapfel, R.W. Ogden, Constitutive modelling of arteries, Proc. R. Soc. A 466 (2010) 1551–1597, doi:10.1098/rspa.2010.0058.

[43] G.A. Holzapfel, H.W. Weizsäcker, Biomechanical behavior of the arterial wall and its numerical characterization, Comput. Biol. Med. 28 (1998) 377–392, doi:10.1016/S0010-4825(98)00022-5.

[44] C.O. Horgan, J.G. Murphy, On the volumetric part of strain-energy functions used in the constitutive modeling of slightly compressible solid rubbers, Int. J. Solids Struct. 46 (2009) 3078–3085, doi:10.1016/j.ijsolstr.2009.04.007.

[45] M.N. Wang, F.J. Liu, A compressible anisotropic hyperelastic model with I5 and I7 strain invariants, Comput. Methods Biomech. Biomed. Eng. 23 (2020) 1277–1286, doi:10.1080/10255842.2020.1795839.

[46] J.G. Murphy, Transversely isotropic biological, soft tissue must be modelled using both anisotropic invariants, Eur. J. Mech. A/Solids 42 (2013) 90–96, doi:10.1016/j.euromechsol.2013.04.003.

[47] Y. Feng, R.J. Okamoto, G.M. Genin, P.V. Bayly, On the accuracy and fitting of transversely isotropic material models, J. Mech. Behav. Biomed. Mater. 61 (2016) 554–566, doi:10.1016/j.jmbbm.2016.04.024.

[48] T.C. Gasser, W.R. Ogden, G.A. Holzapfel, Hyperelastic modelling of arterial layers with distributed collagen fibre orientations, J. R. Soc. Interface 3 (2006) 15–35, doi:10.1098/rsif.2005.0073.

[49] M.A. Hossain, M.S. Islam, Generalized composite numerical integration rule over a polygon using Gaussian quadrature, Dhaka Univ. J. Sci. 62 (2014) 25–29, doi:10.3329/dujs.v62i1.21956.

[50] N.-Y. Yin, P. Fromme, I. McCarthy, H. Birch, Individual variation in Achilles tendon morphology and geometry changes susceptibility to injury, eLife 10 (2021) e63204, doi:10.7554/eLife.63204.

[51] R.F. Ker, Mechanics of tendon, from an engineering perspective, Int. J. Fatigue 29 (2007) 1001–1009, doi:10.1016/j.ijfatigue.2006.09.020.

[52] L.P. Obrezkov, Constitutive Modeling of Hyperelastic Fibrous Material, School of Engineering Science, Lappeenranta University of Technology, 2018 Master's thesis. http://urn.fi/URN:NBN:fi-fe2018090434551

[53] M. Abramowitz, I.A. Stegun, R.H. Romer, Handbook of mathematical functions with formulas, graphs and mathematical tables, Am. J. Phys. 58 (1988) 958, doi:10.1119/1.15378.

[54] P.A. Pękala, B.M. Henry, A. Ochała, P. Kopacz, G. Tatoń, A. Młyniec, J.A. Walocha, K.A. Tomaszewski, The twisted structure of the Achilles tendon unraveled: a detailed quantitative and qualitative anatomical investigation, Scand. J. Med. Sci. Sports 27 (2017) 1705–1715, doi:10.1111/sms.12835.

[55] D. Zupan, M. Saje, On a proposed standard set of problems to test finite element accuracy: the twisted beam, Finite Elem. Anal. Des. 40 (2004) 1445–1451, doi:10.1016/j.finel.2003.10.001.

[56] H. Khayyeri, A. Gustafsson, A. Heuijerjans, M.K. Matikainen, P. Julkunen, P. Eliasson, P. Aspenberg, H. Isaksson, A fibre-reinforced poroviscoelastic model accurately describes the biomechanical behaviour of the rat Achilles tendon, PLoS One 10 (2015) e0126869, doi:10.1371/journal.pone.0126869.

[57] S.A. Maas, A. Erdemir, J.P. Halloran, J.A. Weiss, A general framework for application of prestrain to computational models of biological materials, J. Mech. Behav. Biomed. Mater. 61 (2016) 499–510, doi:10.1016/j.jmbbm.2016.04.012.